Not so smooth after all: resolving dust and gas structures in protoplanetary disks

Cazzoletti, P.

Citation

Cazzoletti, P. (2019, December 12). *Not so smooth after all: resolving dust and gas structures in protoplanetary disks*. Retrieved from https://hdl.handle.net/1887/81821

Author: Cazzoletti, P.
Title: Not so smooth after all: resolving dust and gas structures in protoplanetary disks
Issue Date: 2019-12-12

6 | ALMA survey of Class II protoplanetary disks in Corona Australis: a young region with low disk masses

Cazzoletti, P., Manara, C. F., Hauyu, B. L., van Dishoeck, E. F., Facchini, S.,
Alcalà, J. M., Ansdell, M., Testi, L., Williams, J. P., Carrasco-González, C.,
Dong, R., Forbrich, J., Fukagawa, M., Galván-Madrid, R., Hirano, N.,
Hogerheijde, M., Hasegawa, Y., Muto, T., Pinilla, P., Takami, M., Tamura,
M., Tazzari, M., and Wisniewski, J. P.,
2019, Astronomy and Astrophysics, 626, A11

Abstract

Context. In recent years, the disk populations in a number of young star-forming regions have been surveyed with the Atacama Large Millimeter/submillimeter Array (ALMA). Understanding the disk properties and their correlation with the properties of the central star is critical to understand planet formation. In particular, a decrease of the average measured disk dust mass with the age of the region has been observed, consistent with grain growth and disk dissipation.

Aims. We want to compare the general properties of disks and their host stars in the nearby ($d = 160\,\mathrm{pc}$) Corona Australis (CrA) star forming region to those of the disks and stars in other regions.

Methods. We conducted high-sensitivity continuum ALMA observations of 43 Class II young stellar objects in CrA at 1.3 mm (230 GHz). The typical spatial resolution is $\sim 0.3''$. The continuum fluxes are used to estimate the dust masses of the disks, and a survival analysis is performed to estimate the average dust mass. We also obtained new VLT/X-Shooter spectra for 12 of the objects in our sample for which spectral type information was missing.

Results. 24 disks are detected, and stringent limits have been put on the average dust mass of the non-detections. Taking into account the upper limits, the average disk mass in CrA is $6 \pm 3\,\mathrm{M}_\oplus$. This value is significantly lower than that of disks in other young (1-3 Myr) star forming regions (Lupus, Taurus, Chamaeleon I, and Ophiuchus) and appears to be consistent with the average disk mass of the 5-10 Myr old Upper Sco. The position of the stars in our sample on the Herzsprung-Russel diagram, however, seems to confirm that that CrA has age similar to Lupus. Neither external photoevaporation nor a lower than usual stellar mass distribution can explain the low disk masses. On the other hand, a low-mass disk population could be explained if the disks are small, which could happen if the parent cloud has a low temperature or intrinsic angular momentum, or if the the angular momentum of the cloud is removed by some physical mechanism such as magnetic braking. Even in detected disks, none show clear substructures or cavities.

Results. We conducted high-sensitivity continuum ALMA observations of 43 Class II young stellar objects in CrA at 1.3 mm (230 GHz). The typical spatial resolution is $\sim 0.3''$. The continuum fluxes are used to estimate the dust masses of the disks, and a survival analysis is performed to estimate the average dust mass. We also obtained new VLT/X-Shooter spectra for 12 of the objects in our sample for which spectral type information was missing.

6.1 Introduction

Planets form in protoplanetary disks around young stars, and the way these disks evolve also impacts what kind of planetary system will be formed (Morbidelli and Raymond, 2016). The evolution of the disk mass with time is one of the key ingredients of planetary synthesis models (Benz et al., 2014). For a long time infrared telescopes (e.g., *Spitzer*) have shown how the inner regions of disks dissipate on a timescale of ∼3-5 Myr (Haisch et al., 2001; Hernández et al., 2007; Fedele et al., 2010; Bell et al., 2013).

Only recently, however, we have been able to measure the bulk disk mass for statistically significant samples of disks, thanks to the high sensitivity of the Atacama Large Millimeter/submillimeter Array (ALMA). Pre-ALMA surveys of disk masses were restricted to the northern hemisphere Taurus, Ophiuchus and Orion Nebula Cluster regions (Andrews and Williams, 2005; Andrews et al., 2009, 2013; Eisner et al., 2008; Mann and Williams, 2010). In the first years of operations of ALMA this has changed dramatically: hundreds of disks have been surveyed to determine the disk population in the ∼1-3 Myr old Lupus, Chamaeleon I, Orion Nebula Cluster, Ophiuchus, IC348 and Taurus regions (Ansdell et al., 2016; Pascucci et al., 2016; Eisner et al., 2018; Cieza et al., 2019; Ruíz-Rodríguez et al., 2018; Long et al., 2018), in the ∼3-5 Myr old σ-Orionis region (Ansdell et al., 2017), and in the older ∼5-10 Myr Upper Scorpius association (Barenfeld et al., 2016). These surveys have shown that the typical mass of protoplanetary disks decreases with the age of the region, in line with the observations that the inner regions of disks are dissipated within ∼ 3-5 Myr, similar to the dissipation time scale measured in the infrared. A positive correlation between disk and stellar mass was also found, and a steepening of its slope with time was identified (Ansdell et al., 2016, 2017; Pascucci et al., 2016). This is consistent with the result that massive planets form and are found preferentially around more massive stars e.g. Bonfils et al., 2013; Alibert et al., 2011. Finally, the steepening of the relation with time is explained with more efficient radial drift around low mass stars (Pascucci et al., 2016), and it suggests that a significant portion of the planet formation process, especially around low mass stars, must happen in the first ∼1-2 Myr, when enough material to form planets is still available in disks (Testi et al., 2016; Manara et al., 2018). Studying the evolution of the $\mathrm{M}_{\mathrm{disk}} - \mathrm{M}_{\star}$ relation in as many different environments as possible is therefore critical for understanding how the planet formation process is affected by the mass of the central stars.

We present here a survey of the Class II disks in the Corona Australis star forming region (CrA). Located at an average distance of about 154 pc (Gaia Collaboration et al., 2018b; Dzib et al., 2018), the CrA molecular cloud

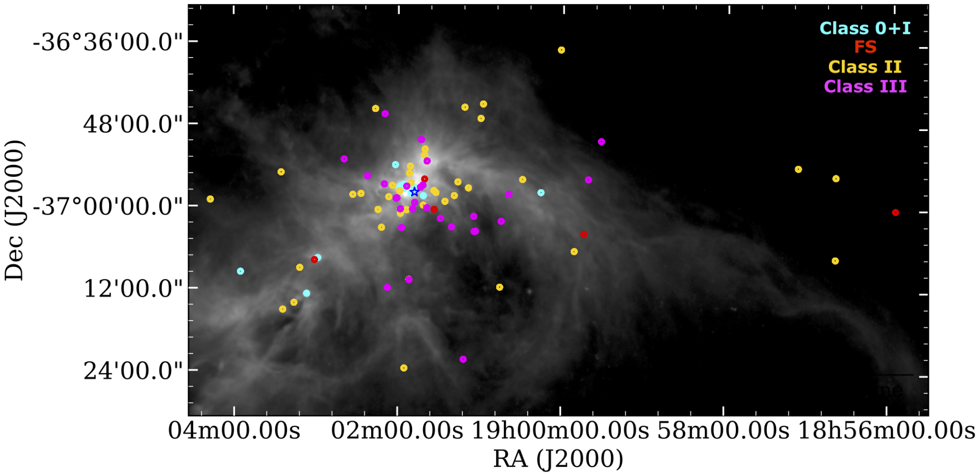

Figure 6.1: Spatial distribution of the CrA sources from the Peterson et al. (2011) catalogue on top of the *Herschel* 250 μm map of the Corona Australis molecular Cloud. The different colours represent the classification of the YSOs. The blue star indicates the position of R CrA

complex is one of the nearest star-forming regions (see review in Neuhäuser and Forbrich, 2008). It has been the target of many infrared surveys, the most recent being the Gould Belt (GB) *Spitzer* Legacy program presented in Peterson et al. (2011). At the center of the CrA region is located the *Coronet* cluster, which is a region of young embedded objects in the vicinity of R CrA (Herbig Ae star, Neuhäuser et al., 2000), on which many of the previous studies have focused. All studies agree in assigning to the *Coronet* an age $< 3\,$Myr (e.g. Meyer and Wilking, 2009; Sicilia-Aguilar et al., 2011). However, there are also some indications of a more evolved population (e.g. Neuhäuser et al., 2000; Peterson et al., 2011; Sicilia-Aguilar et al., 2011). A deep, sub-mm wavelength survey of the disk population in the region can help to further understand the formation and evolutionary history of CrA.

We therefore use ALMA to conduct a high-sensitivity millimeter wavelength survey of all the known Class II sources in CrA and compare the results with other regions surveyed to-date. In Sec. 6.2 the sample is described, while the ALMA observations are detailed in Sec. 6.3. We also describe there new VLT/X-Shooter observations to determine the stellar charachteristics. The continuum millimeter measurements, their conversion to dust masses and a comparison with other star-forming regions is presented in Sec. 6.4. Our findings are interpreted in the context of disk evolution in Sec. 6.5. Finally, the work is summarized in Sec. 6.6.

Table 6.1: Stellar properties of the central sources of the disks in the sample. The RA and DEC in J2000 are from the *Spitzer* data presented in Peterson et al. (2011)

2MASS ID	Name	RA	DEC	SpT	Ref.
J18563974-3707205	CrA-1	18:56:39.76	-37:07:20.8	M6	1
J18595094-3706313	CrA-4	18:59:50.95	-37:06:31.6	M8	2
J19002906-3656036	CrA-6	19:00:29.07	-36:56:03.8	M4	3
J19004530-3711480	CrA-8	19:00:45.31	-37:11:48.2	M8.5	4
J19005804-3645048	CrA-9	19:00:58.05	-36:45:05.0	M1	3
J19005974-3647109	CrA-10	19:00:59.75	-36:47:11.2	M4	5
J19011629-3656282	CrA-12	19:01:16.29	-36:56:28.3	M5	6
J19011893-3658282	CrA-13	19:01:18.95	-36:58:28.4	M2	7
J19013232-3658030	CrA-15	19:01:32.31	-36:58:03.0	M3.5	7
J19013385-3657448	CrA-16	19:01:33.85	-36:57:44.9	M2.5	7
J19014041-3651422	CrA-18	19:01:40.41	-36:51:42.3	M1.5	7
J19015112-3654122	CrA-21	19:01:51.12	-36:54:12.4	M2	8
J19015180-3710478	CrA-22	19:01:51.86	-37:10:44.7	M4.5	1
J19015374-3700339	CrA-23	19:01:53.75	-37:00:33.9	M7.5	7
J19020682-3658411	CrA-26	19:02:06.80	-36:58:41.0	M7	1
J19021201-3703093	CrA-28	19:02:12.00	-37:03:09.4	M4.5	5
J19021464-3700328	CrA-29	19:02:14.63	-37:00:32.9	...	...
J19022708-3658132	CrA-30	19:02:27.07	-36:58:13.1	M0.5	5
J19023308-3658212	CrA-31	19:02:33.07	-36:58:21.2	M3.5	1
J19031185-3709020	CrA-35	19:03:11.84	-37:09:02.1	M5	3
J19032429-3715076	CrA-36	19:03:24.29	-37:15:07.7	M5	1
J19012576-3659191	CrA-40	19:01:25.75	-36:59:19.1	M4.5	1
J19014164-3659528	CrA-41	19:01:41.62	-36:59:52.7	M2	9
J19015037-3656390	CrA-42	19:01:50.48	-36:56:38.4	...	...
J19031609-3714080	CrA-45 E	19:03:16.09	-37:14:08.2	M3.5	1
J19031609-3714080	CrA-45 W	19:03:16.09	-37:14:08.2	M3.5	1
J18564024-3655203	CrA-47	18:56:40.28	-36:55:20.8	M6	1
J18570785-3654041	CrA-48	18:57:07.86	-36:54:04.4	M5	1

Table 6.1: Continues from previous page

2MASS ID	Name	RA	DEC	SpT	Ref.
J19000157-3637054	CrA-52	19:00:01.58	-36:37:06.2	M1	10
J19011149-3645337	CrA-53	19:01:11.49	-36:45:33.8	M5	1
J19013912-3653292	CrA-54	19:01:39.15	-36:53:29.4	K7	9
J19015523-3723407	CrA-55	19:01:55.23	-37:23:41.0	K5	11
J19021667-3645493	CrA-56	19:02:16.66	-36:45:49.4	M4	4
J19032547-3655051	CrA-57	19:03:25.48	-36:55:05.3	M4.5	1
J19010860-3657200	SCrA N	19:01:08.62	-36:57:20	K3	6
J19010860-3657200	SCrA S	19:01:08.62	-36:57:20	M0	6
J19015878-3657498	TCrA	19:01:58.78	-36:57:49	F0	6
J19014081-3652337	TYCrA	19:01:40.83	-36:52:33.88	B9	6
J19041725-3659030	Halpha15	19:04:17.25	-36:59:03.0	M4	12
J19025464-3646191	ISO-CrA-177	19:02:54.65	-36:46:19.1	M4.5	4
...	G09-CrA-9	19:01:58.34	-37:01:06.0	...	...
J19015173-3655143	Haas17	19:01:51.74	-36:55:14.2	...	...
J19020410-3657013	IRS10	19:02:04.09	-36:57:01.2	...	...

References. (1) This work, (2) Bouy et al. (2004), (3) Romero et al. (2012), (4) López Martí et al. (2005), (5) Sicilia-Aguilar et al. (2011), (6) Forbrich and Preibisch (2007), (7) Sicilia-Aguilar et al. (2008), (8) Currie and Sicilia-Aguilar (2011), (9) Meyer and Wilking (2009), (10) Walter et al. (1997), (11) Herczeg and Hillenbrand (2014), (12) Patten (1998)

6.2 Sample selection

Peterson et al. (2011) present in their work a comprehensive catalogue of known Young Stellar Objects (YSOs) in the CrA star forming region selected based on *Spitzer*, 2MASS, *ROSAT*, and *Chandra* data. In addition to the these, they also added more YSOs from the literature. Their final catalogue includes a total of 116 YSOs, 14 of which are classified as Class I, 5 as Flat Spectrum (FS), 43 as Class II and 54 as Class III. The Infrared Class was determined by calculating the spectral slope α over the widest possible range of IR wavelengths as follows:

$$\alpha = \frac{\Delta \log (\lambda F_\lambda)}{\Delta \log \lambda}, \tag{6.1}$$

where λ is the wavelength and F_λ the flux at λ. Sources with $\alpha \geq 0.3$ are classified as Class I; FS have $-0.3 \leq \alpha < 0.3$; Class II have $-1.6 \leq \alpha < -0.3$;

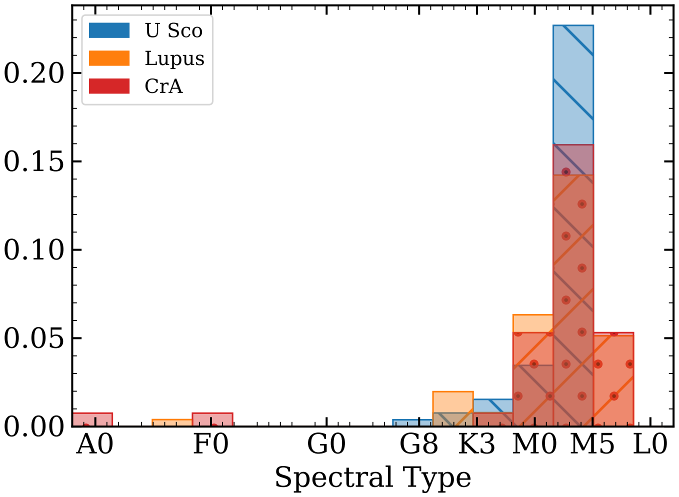

Figure 6.2: Distribution of the spectral types of the stars in CrA (Red) compared to that of Lupus (Orange) and Upper Sco (Blue).

sources with $\alpha < -1.6$ are Class III (Evans et al., 2009; Peterson et al., 2011). Fig. 6.1 shows the spatial distribution of the sources and their classification on top of the *Herschel* 250 μm map of the molecular Cloud.

Our sample includes all the Class II sources from the Peterson et al. (2011) catalogue. Two of them (CrA-49 and CrA-51) were later identified as background, evolved stars based on parallax measurements with Gaia (Gaia Collaboration et al., 2016; Lindegren et al., 2018; Luri et al., 2018; Gaia Collaboration et al., 2018b) and on our VLT/X-Shooter spectra (see Sec. 6.3.2). We then checked our sample against the more recently published survey by Dunham et al. (2015) in which the *Spitzer* data are re-analysed and the spectral slopes re-calculated. We find broad agreement between the classification in Peterson et al. (2011) and Dunham et al. (2015), except for a few very marginal cases at the boundaries of classes.

Our final sample contains 41 targets, two of which are clearly resolved binaries (S CrA and CrA-45). Of the 43 targeted disks, 24 are detected with ALMA. The spectral type (SpT) was known for only 26 of the stars from the literature. We obtained VLT/X-Shooter spectra for 11 of the remaining targets, and derived their properties as explained in Sec. 6.4.1.

The basic stellar properties for the CrA sample are given in Table 6.1, the distribution of SpTs is shown in Fig. 6.2, while the millimeter observations, flux densities, and calculated disk masses are presented in Table 6.3.

6.3 Observations

6.3.1 ALMA observations

We have carried out three executions of observations at 1.3 mm towards 43 Class II YSOs in the Corona Australis molecular cloud, using ALMA (2015.1.01058.S, PI: H. B. Liu).. Each one of the 43 target sources were integrated for approximately 1 minute in each epoch. The spectral setup consists of six spectral windows, of which the (central frequency [GHz], total bandwidth [MHz], and frequency channel width [kHz]) are (216.797, 1875, 488), (219.552, 59, 61), (219.941, 59, 61), (220.390, 117, 61), (230.531, 117, 31), (231.484, 1875, 488), respectively. Additional observational details are summarized in Table 6.2. ^{12}CO (2-1), ^{13}CO (2-1) and C^{18}O (2-1) transitions were also targeted with our spectral setup, but no clear detection was found because of strong foreground contamination. SO (6-5) and SiO (5-4) lines were also covered and not detected.

The data were manually calibrated using the CASA v5.1.1 software package (McMullin et al., 2007) . The gain calibrator for the first epoch of observations was faint. To yield reasonably high signal-to-noise (S/N) ratios when deriving the gain phase solutions, the phase offsets among spectral windows were first solved using the passband calibration scan. After applying the phase offsets solution, the gain phase solution was then derived by combining all spectral windows. The calibration of the other two epochs of observations followed the standard procedure of ALMA quality assurance (i.e., QA2). The bootstrapped flux values of the calibrator quasar J1924-2914 were consistent with the SMA Calibrator list[1] (Gurwell et al., 2007) to ~10%. After calibration, we fit the continuum baseline and subtract it from the spectral line data, using the CASA task `uvcontsub`.

The continuum data imaging was performed with multi-frequency synthesis (MFS) imaging of the continuum data using the CASA-`clean` task, and correcting for the primary beam. By jointly imaging all three epochs of data, for each target source field, the achieved continuum root-mean-square (RMS) noise level is ~0.15 mJy beam^{-1}, and the synthesized beam is $\theta_{\rm maj} \times \theta_{\rm min}$=0.″33×0.″31 (P.A.=67°), corresponding to a spatial resolution of $\sim$ 50 au at $d = 154$ pc. The imaged detections are presented in Fig. 6.3.

It is important to note that because of an error when setting the observation coordinates, the decimal places of the target RAs have been trimmed: this results in an offset of the sources of up to 15″ east of the phase center: as a consequence, our images had to be primary beam corrected. The images in

---

[1] http://sma1.sma.hawaii.edu/callist/callist.html

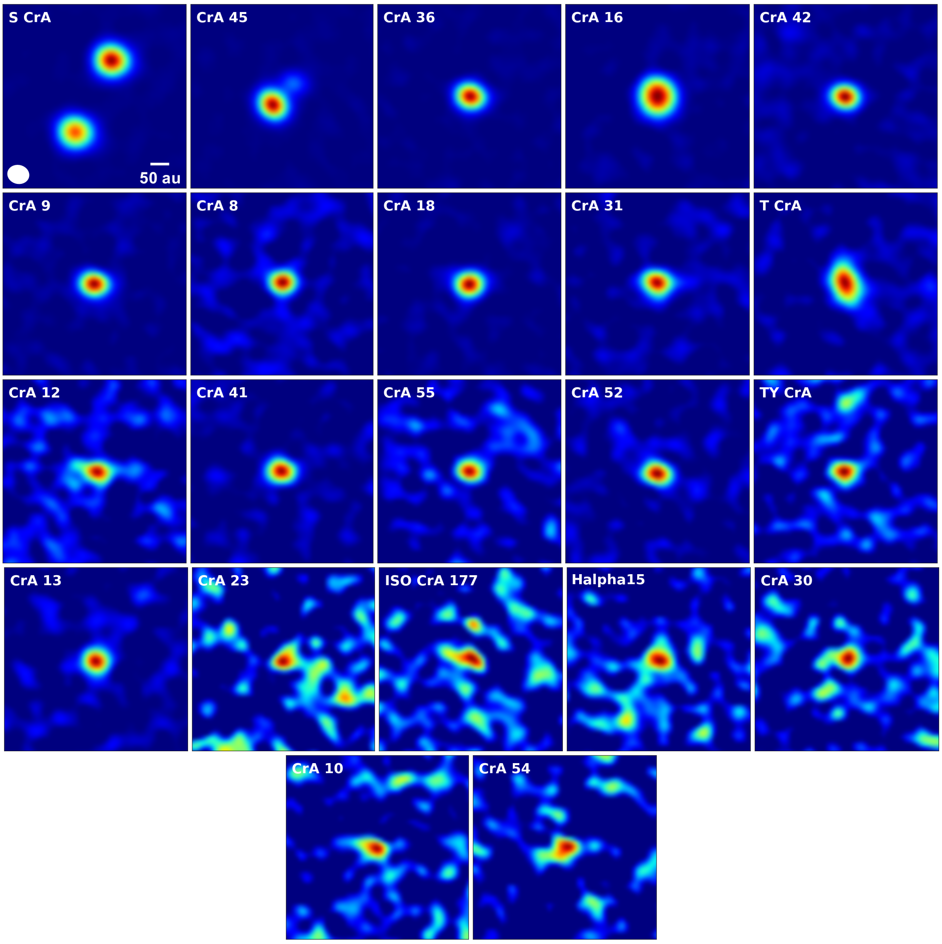

Figure 6.3: ALMA Band 6 1.3 mm continuum images of the 24 detections in Corona Australis. The size of the images is $3'' \times 3''$. The size of the beam is indicated at the bottom-left corner of the first panel ($0''.31 \times 0''.33$). The north of each image is upwards. The presented images have not been primary beam corrected.

Table 6.2: ALMA observations towards Class II objects in the CrA molecular cloud

Epoch	1	2	3
Time (UTC; 2016)	(Aug.01) 03:32-04:54	(Aug.01) 05:01-06:23	(Aug.02) 03:18-04:40
Project baseline lengths (min-max) [m]	14-1108	15-1075	15-1110
Absolute flux calibrator	Pallas	Pallas	Pallas
Gain calibrator	J1937-3958	J1924-2914	J1924-2914
Bootstrapped gain calibrator flux [Jy]	0.26	3.9	4.1
Passband calibration	J1924-2914	J1924-2914	J1924-2914
Bootstrapped passband calibrator flux [Jy]	4.1	3.9	4.1

Fig. 6.3 have therefore been re-centered using the best-fit positions in Tab. 6.3.

6.3.2 VLT/X-Shooter observations

The spectroscopic follow-up observations for the 13 targets with missing spectral type information were carried out in Pr.Id. 299.C-5048 (PI Manara) and Pr.Id. 0101.C-0893 (PI Cazzoletti) with the VLT/X-Shooter spectrograph (Vernet et al., 2011). This instrument covers the wavelength range from ∼300 nm to ∼2500 nm simultaneously, dividing the spectrum in three arms, the UVB ($\lambda\lambda \sim$ 300-550 nm), the VIS ($\lambda\lambda \sim$ 500-1050 nm), and the NIR ($\lambda\lambda \sim$ 1000-2500 nm). All targets were observed both with a narrow slit - 1.0$''$ in the UVB, 0.9$''$ in the VIS and NIR arms - leading to R∼9000 and ∼10000, respectively, and a wide slit of 5.0$''$ used to obtain an accurate flux calibration of the spectra. The log of the observations is reported in Table 6.7. The spectra of all the observed targets are detected in the NIR arm, while only 5 targets are bright enough and not extincted too much to be detected also in the UVB arm.

The reduction of the data was performed using the ESO X-Shooter pipeline 2.9.3 (Modigliani et al., 2010). The pipeline performs the typical reduction steps, such as flat fielding, bias subtraction, order extraction and combination, rectification, wavelength calibration, flux calibration using standard stars observed in the same night. We extracted the 1D spectra from the 2D images produced by the pipeline using IRAF and then removed telluric absorption lines in the VIS and NIR arms using telluric standard stars observed close in time and airmass (see e.g., Alcalá et al. 2014). The S/N of the spectra at different wavelengths is reported in Table 6.7.

6.4 Results and analysis

6.4.1 Stellar properties

The spectral type for the targets were obtained from the literature (see Tab. 6.1) or from the VLT/X-Shooter spectra. The procedure used for the analysis of the X-Shooter spectra was as follows. First, we corrected the spectra for extinction using the values from the literature (Dunham et al., 2015; Sicilia-Aguilar et al., 2008, 2011) and the reddening law by Cardelli et al. (1989) with R_V=3.1, as suggested by Sicilia-Aguilar et al. (2008). Then, we calculated the values of a number of spectral indices both at wavelengths in the VIS and the NIR arms, taken by those calibrated by Riddick et al. (2007), Jeffries et al. (2007), and Herczeg and Hillenbrand (2014), as in Manara et al. (2017), and by Testi et al. (2001), as in Manara et al. (2013). The spectral types derived from these

Table 6.3: 1.3 mm continuum properties of the sources targeted in our sample.

Name	$\Delta\alpha$ [$''$]	$\Delta\delta$ [$''$]	$F_{1.3\,\mathrm{mm}}$ [mJy]	RMS [mJy beam^{-1}]	a_{maj} [$''$]	a_{min} [$''$]	PA [°]	M_{dust} [$M_{\oplus}$]
CrA-1	...	...	...	0.10	...	...	...	...
CrA-4	...	...	...	0.14	...	...	...	...
CrA-6	...	...	...	0.08	...	...	...	...
CrA-8	-0.14	0.39	2.06 ± 0.17	0.16	0.365 ± 0.018	0.31 ± 0.014	81.90 ± 13.3	1.50 ± 0.12
CrA-9	-0.01	0.35	5.07 ± 0.16	0.33	0.389 ± 0.008	0.31 ± 0.005	81.07 ± 3.4	3.70 ± 0.12
CrA-10	0.07	0.34	0.65 ± 0.11	0.22	0.481 ± 0.119	0.25 ± 0.034	73.11 ± 7.9	0.48 ± 0.15
CrA-12	-0.05	0.42	1.37 ± 0.24	0.10	0.661 ± 0.100	0.32 ± 0.030	90.67 ± 4.8	1.00 ± 0.17
CrA-13	0.06	0.27	2.77 ± 0.26	0.21	0.367 ± 0.021	0.35 ± 0.019	126.02 ± 60.2	2.02 ± 0.19
CrA-15	...	...	...	0.08	...	...	...	...
CrA-16	-0.23	0.45	20.34 ± 0.53	1.00	0.478 ± 0.008	0.44 ± 0.007	13.42 ± 11.5	14.84 ± 0.39
CrA-18	-0.20	0.52	5.36 ± 0.19	0.35	0.380 ± 0.008	0.32 ± 0.006	93.93 ± 5.3	3.92 ± 0.14
CrA-21	...	...	...	0.08	...	...	...	...
CrA-22	...	...	...	0.12	...	...	...	...
CrA-23	-0.26	0.76	0.35 ± 0.15	0.12	0.401 ± 0.120	0.28 ± 0.061	108.44 ± 24.8	0.26 ± 0.11
CrA-26	...	...	...	0.11	...	...	...	...
CrA-28	...	...	...	0.09	...	...	...	...
CrA-29	...	...	...	0.11	...	...	...	...
CrA-30	-0.36	0.61	0.51 ± 0.18	0.09	0.504 ± 0.139	0.27 ± 0.046	96.59 ± 10.6	0.37 ± 0.13
CrA-31	-0.28	0.60	2.82 ± 0.19	0.19	0.416 ± 0.019	0.33 ± 0.013	80.58 ± 7.3	2.05 ± 0.14
CrA-35	...	...	...	0.11	...	...	...	...
CrA-36	-0.14	0.38	12.9 ± 0.21	0.82	0.384 ± 0.004	0.32 ± 0.002	74.97 ± 2.1	9.41 ± 0.15
CrA-40	...	...	...	0.11	...	...	...	...
CrA-41	-0.34	0.62	2.80 ± 0.19	0.21	0.384 ± 0.017	0.30 ± 0.011	85.01 ± 6.7	2.04 ± 0.14
CrA-42	-1.00	0.34	4.87 ± 0.21	0.34	0.377 ± 0.010	0.31 ± 0.007	81.88 ± 4.9	3.55 ± 0.16
CrA-45 E	-0.36	0.63	29.82 ± 0.35	1.92	0.400 ± 0.003	0.34 ± 0.002	46.21 ± 1.7	21.76 ± 0.26

Table 6.3: Continues from previous page

Name	$\Delta\alpha$ [″]	$\Delta\delta$ [″]	$F_{1.3\,\mathrm{mm}}$ [mJy]	RMS [mJy beam^{-1}]	a_{maj} [″]	a_{min} [″]	PA [°]	M_{dust} [$M_{\oplus}$]
CrA-45 W	0.05	0.28	6.36 ± 0.34	1.92	0.393 ± 0.013	0.33 ± 0.009	87.43 ± 7.0	4.64 ± 0.25
CrA-47	...	...	...	0.09	...	...	...	...
CrA-48	...	...	...	0.12	...	...	...	...
CrA-52	0.05	-0.27	1.95 ± 0.17	0.16	0.404 ± 0.023	0.29 ± 0.012	70.00 ± 5.4	1.43 ± 0.12
CrA-53	...	...	...	0.10	...	...	...	...
CrA-54	0.61	-0.14	0.48 ± 0.19	0.09	0.577 ± 0.189	0.26 ± 0.044	105.67 ± 7.8	0.35 ± 0.14
CrA-55	-0.26	0.24	0.81 ± 0.14	0.10	0.354 ± 0.037	0.29 ± 0.025	96.62 ± 19.4	0.59 ± 0.10
CrA-56	...	...	...	0.10	...	...	...	...
CrA-57	...	...	...	0.10	...	...	...	...
S CrA S	-0.36	1.34	129.53 ± 2.09	10.4	0.451 ± 0.005	0.40 ± 0.004	75.03 ± 4.3	94.51 ± 1.52
S CrA N	0.23	0.13	140.30 ± 2.00	10.4	0.439 ± 0.004	0.39 ± 0.003	80.73 ± 3.7	102.36 ± 1.46
T CrA	-0.06	1.34	4.99 ± 0.37	0.28	0.568 ± 0.033	0.37 ± 0.016	20.25 ± 4.3	3.64 ± 0.27
TY CrA	0.01	0.46	0.91 ± 0.18	0.13	0.362 ± 0.044	0.28 ± 0.026	90.13 ± 14.6	0.66 ± 0.13
IRS10	...	...	...	0.08	...	...	...	...
Halpha15	-0.07	0.54	0.69 ± 0.22	0.08	0.529 ± 0.128	0.39 ± 0.078	142.60 ± 27.2	0.50 ± 0.16
ISO-CrA-177	-0.01	0.49	0.52 ± 0.17	0.11	0.535 ± 0.146	0.25 ± 0.037	71.91 ± 7.3	0.38 ± 0.13
Haas17	...	...	...	0.11	...	...	...	...
G09-CrA-9	...	...	...	0.09	...	...	...	...

Notes. † Offset with respect to coordinates listed in Tab. 6.1.

indices are presented in Tab. 6.6 in Appendix 6.B. The spectral indices in the VIS arms are more reliable, and we select the spectral type from these indices when available. The observed spectra along with a template of the relative Spectral Types are presented in Fig. 6.8.

The spectral types are converted in effective temperatures ($T_{\rm eff}$) using the relation by Herczeg and Hillenbrand (2014). Stellar luminosity ($L_\star$) is obtained from the reddening-corrected J-band magnitudes and using the bolometric correction from Herczeg and Hillenbrand (2014), assuming for all the target the average distance of 154 pc calculated by Dzib et al. (2018). With this information, we have been able to plot our data on the HR diagram (Fig. 6.6) and to estimate the stellar masses ($M_\star$) for all the targets using the evolutionary tracks by Baraffe et al. (2015) for $M_\star < 1.4 M_\odot$ and Siess et al. (2000) for higher $M_\star$ and ages younger than 1 Myr . The stellar parameters for the targets are reported in Tab. 6.5.

6.4.2 mm continuum emission

Among the 41 targets, 20 of them show a clear ($\geq 4\sigma$) detection within a $1''$ radius from the nominal *Spitzer* location from Peterson et al. (2011). In addition, CrA-42 and T CrA show a $\sim 36\sigma$ and a $\sim 22\sigma$ detection respectively at a slightly larger distance from their nominal *Spitzer* positions ($1''.05$ for CrA-42 and $1''.34$ T CrA), and are also regarded as detections. S CrA is a known binary (Reipurth and Zinnecker, 1993; Ghez et al., 1997; Takami et al., 2003), and we detected millimeter emission associated with both binary components. CrA-45 is also identified as a binary. The total number of detections is therefore 24 out of the 43 targeted disks, so the detection rate is $\sim 56\%$.

None of the disks show clear substructures, no transition disk with cavities with radius $> 25\,$au are found and all of them appear to be unresolved or marginally resolved: a Gaussian is therefore fitted to the detected sources (two Gaussians for the binaries) in the image plane using the `imfit` task in `CASA`. The task returns the total flux-density $F_{1.3\,\rm mm}$ of the source along with the statistical uncertainty, the FWHM along the semi-major ($a_{\rm maj}$) and semi-minor ($a_{\rm min}$) axis and the position angle (PA). The results of the fit are shown in Table 6.3[2]The right ascension offset ($\Delta\alpha$) and the declination offset ($\Delta\delta$) with respect to the *Spitzer* coordinates is also shown. The rms noise for the non-detections was calculated using the `imstat` task within a $1''$ radius centered at the *Spitzer* coordinates; for the detection, it was calculated in an annular region centered on the source and with inner and outer radii equal to $2''$ and $4''$, respectively.

---

[2] Note that the $F_{1.3\,\rm mm}$ uncertainty only includes the statistical uncertainty from the fit, and not the 10% absolute flux calibration uncertainty.

In order to constrain the average flux density of individually undetected sources, a stacking analysis was also performed. The images were centered at their *Spitzer* coordinates (Table 6.1) and then stacked. Even after the stacking, no detection was found and an average rms noise is $0.017\,\mathrm{mJy\,beam^{-1}}$, corresponding to a 3σ upper limit of $0.051\,\mathrm{mJy}$ is found assuming unresolved disks. However, it should be noted that the average offset between the disks and the *Spitzer* positions, measured on the detections, are $<\Delta\alpha>= -0.13''$ and $<\Delta\delta>= 0.47''$: it is therefore possible that the undetected sources did not overlap during the stacking, and that the upper limit is actually higher than that quoted.

6.4.3 Dust masses

Assuming that the observed sub-millimeter emission is optically thin and isothermal, the relation between the emitting dust mass (M_{dust}) and the observed continuum flux at frequency ν (F_ν) is as follows (Hildebrand, 1983):

$$M_{\mathrm{dust}} = \frac{F_\nu\, d^2}{\kappa_\nu\, B_\nu(T_{\mathrm{dust}})} \approx 2.19 \times 10^{-6} \left(\frac{d}{160}\right)^2 F_{1.3\,\mathrm{mm}}\,[\mathrm{M_\odot}], \qquad (6.2)$$

where d is the distance of the object, F_ν is measured the flux-density, $B_\nu(T_{\mathrm{dust}})$ is the Planck function for a given dust temperature T_{dust} and κ_ν is the dust opacity at frequency ν. To make the comparison with previous surveys easier, for the dust opacity κ_ν we follow the same approach of Ansdell et al. (2016), assuming $\kappa_\nu = 10\,\mathrm{cm^2\,g^{-1}}$ at 1000 GHz (Beckwith et al., 1990) and scaling it to our frequency using $\beta = 1$. The adopted value is therefore $\kappa_\nu = 2.3\,\mathrm{cm^2\,g^{-1}}$ at $\nu = 230\,\mathrm{GHz}$ (1.3 mm). In the right-hand side of Eq. 6.2, the distance d is measured in pc and the flux density $F_{1.3\,\mathrm{mm}}$ is in mJy. For each object, the average distance of the cluster $d = 154$ pc was used. For the dust temperature, we use a constant $T_{\mathrm{dust}} = 20\,\mathrm{K}$ (Andrews and Williams, 2005), rather than the $T_{\mathrm{dust}} = 25\,\mathrm{K} \times (L_*/L_\odot)^{0.25}$ relation based on two-dimensional continuum radiative transfer by Andrews et al. (2013) and used in other works (e.g. Law et al., 2017). We adopt this simplified approach with a single grain opacity and temperature for all the disks in the sample following the approach of Ansdell et al. (2016) and to facilitate the comparison with other star-forming regions (see Sec. 6.4.4). Moreover, it should be noted that no dependence of the average dust temperature on the stellar parameters was found with the more detailed modelling by Tazzari et al. (2017) for the Lupus disks.

The dust masses of the disks in our sample are presented in Tab. 6.3, along with the relative uncertainty calculated from the flux uncertainty. Only

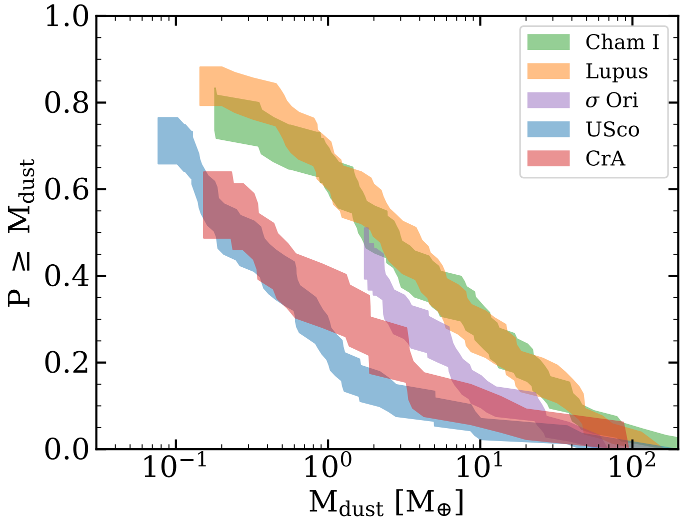

Figure 6.4: Comparison of the cumulative dust mass distributions of Lupus, CrA, Cham I, σ Ori and Upper Sco, derived using a survival analysis accounting for the upper limits.

3 disks out of 24 detections have a dust content $\geq 10\,\mathrm{M}_\oplus$[3] and large enough to form the cores of giant planets in the future. However, it is still possible that a similar amount of dust mass is hidden at the inner few region due to very high optical depth (e.g. Zhu et al., 2010; Liu et al., 2017; Vorobyov et al., 2018). Also note that very recent high angular resolution ALMA and VLA observations of disks are revealing that an important amount of dust is located in dense regions such as rings (e.g. Andrews et al., 2018), which are optically thick at wavelengths around 1 mm (Dullemond et al., 2018). When optically thin emission is detected, higher masses are estimated (Carrasco-González et al., 2016).

The stacking of the non-detections gives an average 3σ upper limit corresponding to $0.036\,\mathrm{M}_\oplus$, about 3 Lunar masses.

6.4.4 Comparison with other regions

The surveys of nearby star forming regions over the last years have shown growing evidence of a decrease in the mass of the disks with age, reflecting dust growth and disk dispersal. Ansdell et al. (2016, 2017) found consistent results, calculating the highest average mass in the youngest regions (1-3 Myrs),

---

[3] 5 sources in total have a dust content $\geq 10\,\mathrm{M}_\oplus$ if we also consider CrA-16 and CrA-36, which have dust masses only marginally below $10\,\mathrm{M}_\oplus$.

Table 6.4: Global properties of the star forming regions surveyed with ALMA in order of age.

Name	Distance [pc]	Age [Myr]	Average dust mass [$M_\oplus$]
Taurus	129.5^1	1-3	13 ± 2
Lupus	$160^{1,\star}$	1-3	14 ± 3
CrA	$154\ ^1$	1-3	6 ± 3
Chameleon I	192^1	2-3	24 ± 9
IC 348	321^1	2-3	4 ± 1
σ Ori	388^1	3-5	7 ± 1
Upper Sco	144^3	5-10	5 ± 3

References. (1) Dzib et al. (2018) (2) Comerón (2008) (3) de Zeeuw et al. (1999) $\star$ The average distance of the 4 Lupus clouds was used.

and the lowest for the the oldest Upper Sco association (5-10 Myrs). The 2-3 Myrs old IC348 is the only exception, showing an average dust mass of only $4 \pm 1\,\mathrm{M}_\oplus$ (between the average σ Orionis and that of Upper Sco) despite its young age. This can be explained by the low-mass stellar population in the region (Ruíz-Rodríguez et al., 2018) (also see Tab. 6.4).

The same analysis was done here for CrA. The dust masses are uniformly calculated following the approach used by Ansdell et al. (2016), namely using Eq. 6.2 with the continuum fluxes (or the $3\,\sigma$ upper limits) from our ALMA data or from the literature, assuming a uniform $T = 20\,\mathrm{K}$, and inputting the frequency of the observation for each specific dataset. The distances assumed for each region are listed in Tab. 6.4. For the Upper Sco region, only the disks classified as "full", "evolved" and "transitional" from the Barenfeld et al. (2016) sample are included, while the "debris" and Class III YSOs, which likely represent a separate evolutionary stage, are excluded. Finally, in order to facilitate the comparison with the other samples, in this analysis we only include the disks around stars with masses above the brown-dwarf limit ($M_\star \geq 0.1\,\mathrm{M}_\odot$). The Kaplan-Meier estimator from the `lifelines`[4] and `ASURV` (Lavalley et al., 1992) packages were then used to estimate the cumulative mass distribution and to calculate the average dust mass and its uncertainty while properly accounting for the upper limits by using well-established techniques for left-censored data sets.

Fig. 6.4 presents the results accounting for the upper limits given by the

---

[4] 10.5281/zenodo.1495175

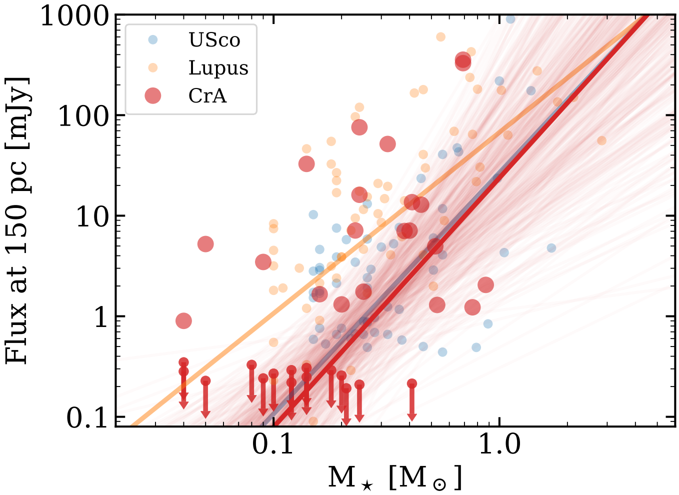

Figure 6.5: Correlation between dust disk flux scaled at 330 GHz (assuming $\alpha = 2.25$, as in Ansdell et al., 2018) and at a distance of 150 pc with stellar mass for the objects in CrA. The slopes of Lupus and Upper Sco are also plotted for comparison. We show the results of the Bayesian fitting procedure by Kelly (2007). The solid line represents the best fit model, while the light lines show a subsample of models from the chains, giving an idea of the uncertainties.

non-detections. With an average dust mass of $6 \pm 3\,\mathrm{M}_\oplus$, the distribution of the CrA disks appear closer to that of the old Upper Sco region rather than to those of the younger systems.

6.4.5 $M_{\rm disk} - M_\star$ relation

A clear correlation between the dust mass of disks and the mass of the central star has been identified across all protoplanetary disk populations surveyed (Pascucci et al., 2016; Ansdell et al., 2017). This finding highlights how the disk properties are affected by the central star, and is consistent with the correlation between frequency of giant planets and mass of the host star, both from the observational and theoretical points of view (Alibert et al., 2011; Bonfils et al., 2013). Moreover, the slope of this relation has been observed to steepen with time, with the young Taurus, Lupus and Chemeleon I regions ($\sim 1 - 3\,$Myr) having slopes similar to each other and shallower than that found for the disks in the Upper Sco association ($5 - 10\,$Myr).

Studying the $M_{\rm dust} - M_\star$ relation for the disks in the CrA sample contributes to gain insight on the origin of the overall low mass of the disk population found in Sec. 6.4.4. We derive the $M_{\rm dust} - M_\star$ relation using the same linear-regression Bayesian approach followed by Ansdell et al. (2017) and presented by Kelly (2007)[5]. Unlike other linear regression methods, this approach is capable of simultaneously accounting for the uncertainties in both the measurements of M_{dust} and $M_\star$, of the intrinsic scatter of the data and of the disk non detections, which result in upper-limits on the disk masses. Note that the SpT, and therefore the stellar mass, is missing for 5 of our targets: for these objects the stellar mass is randomly drawn from the stellar mass distribution of the entire sample. In particular, 4 of the objects with unknown SpT are also not detected with ALMA, while the other one (CrA-42) shows a clear detection of a disk at mm-wavelengths. For the 4 non detections, the stellar mass is therefore randomly drawn among the masses of the stars with non-detected disks, while the mass of CrA-42 is drawn from those showing a detection with ALMA. This uncertainty is also taken into account in the Bayesian approach we adopt by performing 100 different draws. In our fit, a standard uncertainty of 20% of $M_\star$ on the stellar mass is assumed (Alcalá et al., 2017; Manara et al., 2017), while the uncertainties shown in Tab. 6.3 were used for the M_{dust} values. Finally, it should be noted that only 1 out of 89 sources in Lupus was a Herbig Ae/Be star, while Upper Sco did not include any Herbig. We therefore decided not to include T CrA and TY CrA in the fit , for which the $M_{\mathrm{dust}} - M_\star$ relation might not hold.

The best fit relation we find is then plotted in Fig. 6.5 in dark red, along with a subsample of all the models in the chains to show the uncertainty. As in the other surveys, we also find a correlation, where the best-fit model has a slope $\beta = 2.32 \pm 0.77$ and intercept $\alpha = 1.29 \pm 0.60$. This regression intercept is lower that that of other regions, as a consequence of the low disk masses found in the region. The uncertainties of the best-fit parameters reflect the large scatter in the data and the low number statistics.

In order to test that no strong bias was introduced by our procedure, we also run the fit described above without any random draw, finding consistent results.

6.5 Discussion

6.5.1 Is CrA old?

The observed low disk dust masses suggest that the CrA objects targeted in our survey may have an age comparable to that of the Upper Sco association, rather than to the young Lupus region. Unlike CrA, however, Upper Sco shows

---

[5] https://github.com/jmeyers314/linmix

no presence of Class 0 or Class I sources, as expected for a $5 - 10$ Myr region (Dunham et al., 2015). Moreover, most studies agree in assigning Corona Australis an age < 3 Myr (e.g. Meyer and Wilking, 2009; Nisini et al., 2005; Sicilia-Aguilar et al., 2008, 2011).

On the other hand, most of these studies focused only on the *Coronet* cluster, a small region extending ~ 1 pc around the R CrA YSO, and where most of the young embedded Class 0 and Class I sources are located (see Fig. 6.1). The hypothesis that the large scale YSO population of the whole CrA cloud also includes a population of older objects therefore cannot be entirely ruled out. Some evidence of an additional older population has already been presented in previous studies. Neuhäuser et al. (2000) for example identify two classical T Tauri stars located outside the main cloud with an age of ~ 10 Myr using ROSAT data. In addition, Peterson et al. (2011) perform a clustering analysis of the 116 YSOs in their sample, identifying a single core (corresponding to the *Coronet*) and a more extended population of PMS stars showing an age gradient west of the *Coronet*. They also observe that in the central core, the ratio Class II/ Class I=1.8, while the same ratio is Class II/ Class I=2.3 when all the objects in the sample are considered, again hinting toward a younger

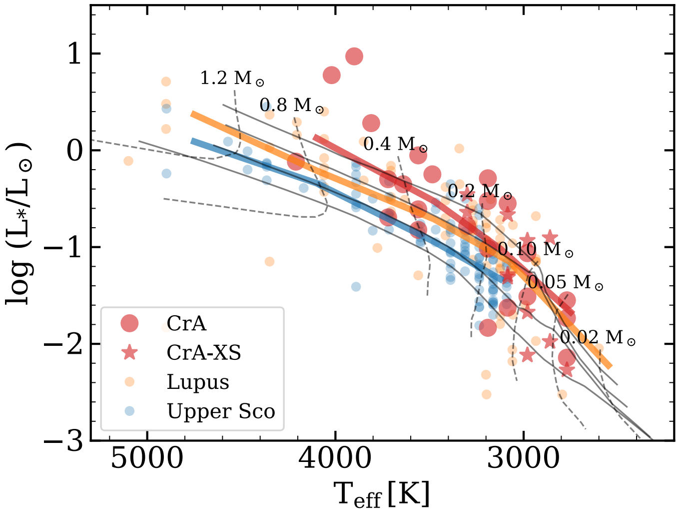

Figure 6.6: HR diagram showing the sources in our CrA sample (red), in the Lupus sample from Ansdell et al. (2016) (orange) and in the Upper Sco sample (blue) from Barenfeld et al. (2016). The evolutionary tracks for different stellar masses and the relative isochrones from Baraffe et al. (2015) are also plotted for reference. The isochrones refer (from top to bottom) to the 1 Myr, 2Myr, 5 Myr and 10 Myr isochrone. The coloured solid lines show the approximate median value of the luminosity at each temperature.

population inside the *Coronet*. Finally, Sicilia-Aguilar et al. (2011) point out that the relatively low disk fraction observed in the *Coronet* ($\sim$ 50% López Martí et al., 2010, based on near IR photometry) is in strong contrast with the young age of the system: this inconsistency could be solved if an older population were also present. The large scatter in the $M_{\rm dust} - M_\star$ relation could also be a consequence of two stellar populations of different ages.

In order to further test if the Class II population in our sample indeed includes an older population, we have placed them on the HR diagram, by using the spectral types listed in Tab. 6.1 and by deriving effective temperatures and bolometric corrections using the relationships in Herczeg and Hillenbrand (2014) and tables in Herczeg and Hillenbrand (2015), respectively. The obtained diagram is presented in Fig. 6.6. For comparison, the Upper Sco and Lupus objects are also plotted. In contrast with what Fig. 6.4 suggests, the HR diagram supports the scenario of a young CrA cluster with an age more consistent to that of Lupus than to Upper Sco.

In order to make this conclusion evident, the median values of the bolometric luminosities for each temperature are also shown (solid coloured lines in Fig. 6.6). The indicative age of the cluster is the isochrone closer to those median values: these lines also suggest that CrA is younger than Upper Sco. However, a more extended spectral classification for a larger number of objects in CrA would be needed to fully test this older-population scenario.

6.5.2 Is CrA young?

If the whole CrA is coeval with an age of $1-3\,$Myr, some other mechanism has to be invoked to explain the low observed mm fluxes. For example, these fluxes could be due to low metallicity. However, James et al. (2006) determined metallicities for three T Tauri stars in CrA, finding them to be only slightly sub-solar, and not low enough to explain our obesrvations.

External photo-evaporation is also known to play an important role in the disk mass evolution (Facchini et al., 2016; Winter et al., 2018b), and evidence of it occurring has been found in σ Ori (Maucó et al., 2016; Ansdell et al., 2017), where a clear correlation between disk mass and distance from the central Herbig O9V star has been observed and in the Orion Nebula Cluster (Mann and Williams, 2010; Eisner et al., 2018). However, in CrA no correlation between the mass of the disks (or the disk detection rate) and the distance from the brightest star (R CrA) is found. Moreover, in σ Ori external photo-evaporation has been shown to affect disks up to 2 pc away from the Herbig star, where the geometrically diluted far-ultraviolet (FUV) flux reached a value of $\sim 2000\,G_0$. The spectral type of R CrA is still uncertain, ranging from F5 (e.g. Garcia

Lopez et al., 2006) to B8 (e.g. Hamaguchi et al., 2005). Even in the latter case, assuming a typical FUV luminosity for a B8 star of $L_{\mathrm{FUV}} \sim 10\,\mathrm{L}_{\odot}$ (Antonellini et al., 2015) and accounting for geometric dilution, we find that the FUV flux would drop to $\sim 1\,G_0$ in the first inner pc from R CrA, thus ruling-out external photo-evaporation as an explanation. Also, this calculation neglects dust absorption, which is probably very effective in the Coronet cluster around R CrA.

Because of the $\mathrm{M_{disk}} - \mathrm{M_{\star}}$ relation presented in Sec. 6.4.5, it is also possible that a system dominated by low-mass stars shows a low-mass disk population, regardless of its age, as in the case of IC348 (Ruíz-Rodríguez et al., 2018). It is therefore important, when comparing disk dust masses from different regions, to verify that they have the same stellar mass distribution. In order to do this, we employ a Monte Carlo (MC) approach similar to that used by Andrews et al. (2013). We first normalize the stellar populations by defining stellar mass bins and randomly drawing the same number of sources in each bin from the reference sample (CrA) and from a comparison sample (Lupus, Chamaeleon I or Upper Sco). We then perform a two-sample logrank test for censored datasets between the disk dust masses of the two samples, to test the probability (p_{ϕ} value) that the two samples are randomly drawn from the same parent population. A low p_{ϕ} value indicates that the difference in disk masses cannot only be ascribed to different stellar populations and that some other factor, such as disk evolution and the age of the system, must play a role. This process is repeated 10^4 times, and the results are used to create the cumulative distributions shown in Fig. 6.7. When using Upper Sco as a comparison sample, we find a median p_{ϕ} value of 0.53, while the median p_{ϕ} for Lupus is only 0.004. The conclusion is that even when accounting for the $\mathrm{M_{dust}} - \mathrm{M_{\star}}$ relation, the disk dust mass distribution of CrA appears to be statistically different from that of Lupus, while it is significantly more similar to that from that of Upper Sco. Therefore, the comparably low masses of the protoplanetary disks in CrA cannot be explained in terms of the low stellar masses.

Another way a disk can lose part of its mass is via tidal interaction with other stars (e.g. Clarke and Pringle, 1993; Pfalzner et al., 2005). This mechanism is, however, only effective in much denser environments than CrA (e.g. Winter et al., 2018a). In principle, it is possible to imagine that at very early stages most of the stars were located in a dense region (e.g. the *Coronet*) where they interacted violently before being ejected. However, the very low velocity dispersion of the stars in the cluster makes this scenario very unlikely (Neuhäuser et al., 2000). Tidal interaction can be effective in removing dust mass from a disk even in later stages when the disk is in a binary system (e.g.

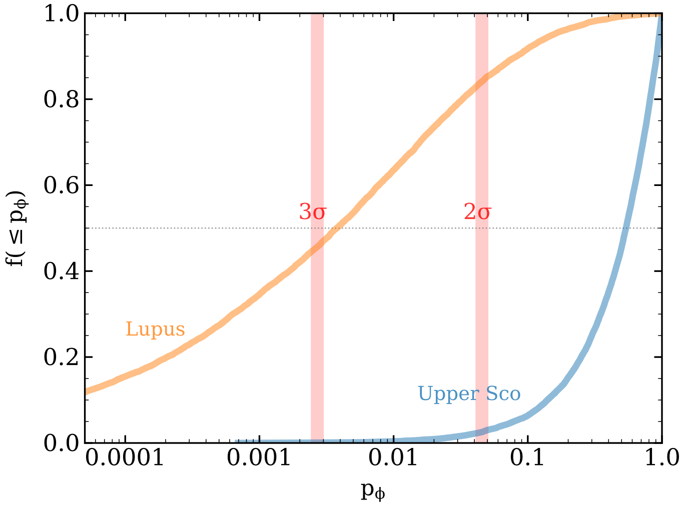

Figure 6.7: Comparison of the mass distributions of Lupus and USco to that of CrA, following the MC analysis proposed by Andrews et al. (2013). p_ϕ is the probability that the synthetic population drawn from the comparison sample (Lupus and Upper Sco) and the reference sample come from the same parent population. $f(< p_\phi)$ is the cumulative distribution for p_ϕ resulting from the logrank two-sample test for censored datasets after 10^4 MC iterations.

Artymowicz and Lubow, 1994), as proposed to explain the low mm flux of some objects in Taurus by Long et al. (2018). A higher than usual binary fraction could therefore explain the low disk masses observed in CrA. However, Ghez et al. (1997) show that the binary fraction of CrA is indistinguishable from those of Lupus and Chameleon I.

Finally it is possible that the low mass distribution observed today is a consequence of a population of disks that has formed with a low mass from the very beginning. For example, the disk formation efficiency in a cloud with mass M_0 depends on the sound speed c_s and on the solid body rotation rate Ω_0, where we have defined the disk formation efficiency as the fraction of M_0 that is in the disk at the end of the collapse stage, or as the ratio between $M_\mathrm{disk}/M_\star$ at that time (Cassen and Moosman, 1981; Terebey et al., 1984). In particular, clouds with higher c_s and Ω_0 (i.e. warmer or more turbulent) will form more massive disks (also see Appendix A in Visser et al., 2009). Therefore, a cold parent cloud or one with low intrinsic angular momentum Ω_0, will form disks with a lower mass, and with a lower $M_\mathrm{disk}/M_\star$ as observed in CrA. Consistently, observations of dense cloud cores in the CrA cloud show line-widths lower than in other regions (Tachihara et al., 2002). Moreover, because of the smaller circularization radius, the formed disks would alse be smaller (e.g. Dullemond et al., 2006) and potentially mostly optically thick, thus hiding an even larger fraction of the mass . Alternatively, small and optically thick disks could result from magnetic braking of the disks by means of the magnetic field threading the disk and the surrounding molecular cloud at the formation stage (e.g. Mellon and Li, 2008; Herczeg and Hillenbrand, 2014; Krumholz et al., 2013). The same scenario was proposed by Maury et al. (2019) to explain the low occurrence of large ($> 60\,\mathrm{AU}$) Class 0 disks in the CALYPSO sample.

Such scenarios, although not testable with the present dataset, are consistent with the low disk mass distribution and with the low intercept of the $\mathrm{M_{disk}} - \mathrm{M_\star}$ in CrA and are not in contradiction with the young age of the stellar popultion. If the parent cloud initial conditions are indeed responsible for the low masses observed, this would be an additional critical aspect to be considered when studying planet formation and evolution. Since the conditions at the epoch of disk formation can be different in each star-forming region, proper modelling is required to assert to which extent they can affect the initial disk mass distribution, the subsequent disk evolution, planet formation and planetary populations.

Observationally, this could be tested by observing the mass of disks around Class 0 and Class I objects in CrA: if the disks are born with a low-mass, the disk mass distribution even at these younger stages should be significantly lower than in other regions.

6.6 Conclusion

We presented the first ALMA survey of 43 Class II protoplanetary disks in the Corona Australis nearby ($d = 160\,\mathrm{pc}$) star forming region, in order to measure their dust content and understand how it scales with the stellar properties. The ultimate goal was to test if the relations between disk properties, age of the stellar population found in other surveys also hold for this region.

1. The average mm fluxes from the disks in CrA is low. This in turn converts into a low disk mass distribution. Even though our observations are able to constrain dust masses down to $\sim 0.2\,\mathrm{M_\oplus}$, the detection rate is only 56%. Moreover, we find that only 3 disks in our sample have a dust mass $\geq 10\,\mathrm{M_\oplus}$ and thus sufficient mass to form giant planet cores.

2. We obtained VLT/X-Shooter spectra for 8 objects with previously unknown spectral type, and derived their stellar physical properties.

3. Despite the apparent young age of the CrA stellar population, we find that the dust mass distribution of the disks in CrA is much lower than that of the Lupus young star forming region which shares a similar age, while it appears to be consistent with that in the 5-10 Myr old Upper Sco association. The correlation between disk dust mass $M_{\rm dust}$ and stellar mass $M_\star$ previously identified in all other surveyed star forming regions is confirmed. However, because of the low mass of the disks in our sample we find a much lower intercept. The large scatter of the data points does not allow the slope of the relation to be well constrained for CrA.

4. Since most of the age estimates of the CrA regions are based on the population of the compact *Coronet* cluster, a possible explanation for the low disk masses might be in principle that CrA also hosts an old population of disks, consistently with previous observations. The position of the objects of our sample on the HR diagram, however, seems to support the idea of a mostly coeval, young population.

5. Low disk masses in a young star forming region can be explained by external photo-evaporation (as in the case of σ Ori) or by a low stellar mass population (as in IC348). With our analysis, we can rule out both these scenarios for CrA. Tidal interaction between different members of CrA, stripping material from the disks, as well as close binaries can also be ruled out.

6. We suggest that initial conditions may play a crucial role in setting the initial disk mass distribution and its subsequent evolution. Small disks with low mass can originate from a cloud with very low turbulence or sound speed, or can alternatively result from disk magnetic braking. It is therefore important to better study the impact of initial conditions on the disk properties, especially if planet formation occurs even before 1 Myr age, as the recent results from Tychoniec et al. (2018) and Manara et al. (2018) suggest.

Future surveys including younger Class 0 and I objects in CrA and other star forming regions will help testing wether or not initial conditions play a critical role in shaping the physical properties of circumstellar disks.

6.A Additional stellar properties

Tab. 6.5 shows a compilation of the most relevant stellar parameters used in our analysis. The *J* magnitude is taken from the 2MASS survey (Cutri et al., 2003).

The extinctions are either derived from our VLT/X-Shooter spectra or from the references in Column 4. Note that the extinctions from Dunham et al. (2015) were not derived from the stellar spectra but from extinction maps and might therefore systematically overestimate the real extinction towards the star by 1-2 mag (see Sec. 4.1 in Peterson et al., 2011). In order to make sure that the extinction values from Dunham et al. (2015) were accurate, we compared them to those derived from the spectra by Sicilia-Aguilar et al. (2011) for 8 targets common to the two samples. We found that the extinctions derived with the two methods are consistent within the uncertainties. The effective temperatures and bolometric luminosities have finally been derived as explained in Sec. 6.5.1 and then used to determine the stellar masses as explained in Sec. 6.4.1.

Table 6.5: Compilation of the most relevant stellar properties used in our analysis. Only the stars with known Spectral Type were included.

Source	J [mag]	A_v [mag]	Ref.	T_eff [K]	$\log L_\star/L_\odot$	$M_\star$ [$M_\odot$]
CrA-1	10.99	0.0	1	2860	-0.90	0.10^s
CrA-4	13.98	3.3	2	2770	-1.73	0.04^b
CrA-6	10.77	2.2	2	3190	-0.52	0.21^b
CrA-8	12.92	1.2	2	2770	-1.55	0.05^b
CrA-9	10.38	2.1	2	3720	-0.29	0.45^b
CrA-10	14.19	2.7	3	3190	-1.83	0.16^b
CrA-12	12.95	1.4	2	2980	-1.51	0.09^b
CrA-13	12.83	8.1	3	3560	-0.61	0.38^b
CrA-15	14.85	14.0	3	3300	-0.78	0.24^b
CrA-16	14.45	17.0	3	3485	-0.24	0.32^b
CrA-18	13.90	14.0	3	3640	-0.35	0.41^b
CrA-21	14.91	13.5	3	3560	-0.82	0.41^b
CrA-22	12.33	1.1	1	3085	-1.28	0.14^b
CrA-23	14.08	0.08	3	2770	-2.14	0.04^b
CrA-26	15.58	4.2	1	2770	-2.26	0.04^b
CrA-28	13.41	1.9	3	3085	-1.62	0.12^b
CrA-30	9.31	3.3	2	3810	0.28	0.53^s
CrA-31	10.59	2.0	1	3300	-0.45	0.23^b
CrA-35	12.03	2.1	2	2980	-1.06	0.12^b
CrA-36	14.57	12.1	1	2980	-0.93	0.14^b
CrA-40	11.61	4.0	1	3085	-0.66	0.18^b
CrA-41	10.46	4.7	3	3560	-0.05	0.40^b

Table 6.5: Continues from previous page

Source	J [mag]	A_v [mag]	Ref.	T_eff [K]	$\log L_\star/L_\odot$	$M_\star$ [$M_\odot$]
CrA-45	11.91	5.0	1	3300	-0.63	0.24^b
CrA-47	13.67	0.0	1	2860	-1.97	0.05^b
CrA-48	14.06	0.0	1	2980	-2.11	0.08^b
CrA-52	10.82	0.2	3	3720	-0.69	0.52^b
CrA-53	13.38	1.5	1	2980	-1.67	0.09^b
CrA-54	7.60	1.4	3	4020	0.77	0.76^s
CrA-55	9.78	1.0	3	4210	-0.11	0.87^b
CrA-56	12	2.2	3	3190	-1.01	0.20^b
CrA-57	12.31	0.8	1	3085	-1.31	0.14^b
SCrA N	8.49*	7.9	2	3900	0.97	0.69^s
SCrA S	8.49*	7.9	2	3900	0.97	0.69^s
TCrA	8.93	7.9	2	7200	1.46	2.25^s
TYCrA	7.49	7.9	2	10500	2.47	4.10^s
Halpha15	11.82	0.8	4	3190	-0.28	0.25^s
ISO-CrA-177	12.44	0.5	5	3085	-0.54	0.20^s

A_v references. (1) This work (2) Dunham et al. (2015) (3) Sicilia-Aguilar et al. (2011) (4) Patten (1998) (5) López Martí et al. (2005)
Evolutionary Tracks. (s) Siess et al. (2000) (b) Baraffe et al. (2015)

6.B VLT/X-Shooter Spectra

In this section we present the VLT/X-Shooter spectra obtained (Fig. 6.8). The Spectral Types derived from the different spectral indices calibrated are presented in Tab. 6.6. In particular, SpT VIS was obtained from the average values from Riddick et al. (2007), as in Manara et al. (2013, 2017); SpT TiO was obtained with the index by Jeffries et al. (2007); SpT NIR was obtained with the indices by Testi et al. (2001), as in Manara et al. (2013); the uncertainties represent the spread between the different indices in the VIS and NIR arms. The adopted spectral types, reported in the last column of Tab. 6.6, are taken from the indices calculated in the VIS arm of the spectrum. In addition, the log of the our X-Shooter observations is presented in Tab. 6.7 along with the Signal to Noise ratio achieved at different wavelengths.

Table 6.6: Spectral types derived from different spectral indices

Source	SpT VIS	SpT TiO	SpT NIR	SpT
CrA-1	M6.05±1.3	M5.46	M7.70±1.3	M6
CrA-22	M3.74±2.1	M4.48	M5.54±2.1	M4.5
CrA-26	M6.68±1.7	M0.64	L1 ±1.7	M7*
CrA-31	M3.66±3.0	M3.61	M7.96±3.0	M3.5
CrA-36	M4.86±2.3	M2.84	L1 ±2.3	M5*
CrA-40	M3.07±1.6	...	M6.42±1.6	M4.5*
CrA-42	M4.44±3.5	...	L2 ±3.5	...
CrA-45	M3.56±1.3	M2.22	M5.37±1.3	M3.5
CrA-47	M5.74±2.0	M5.87	L0.92±2.0	M6
CrA-48	M3.17±2.1	...	M5.22±2.1	M5*
CrA-53	M5.02±1.1	M5.13	M7.90±1.1	M5
CrA-57	M4.05±1.8	M4.57	M5.89±1.8	M4.5
IRS10	...	...	L1.87±5.4	...

$\star$ Uncertain estimate of SpT due to the low S/N of the spectra.

Table 6.7: Night log and basic information on the spectra. In Column 1 is the name of the source, in Column 2 the date and time of the observations, in Column 3-5 the exposure times, in Column 6-8 the slit widths, in Column 9-11 the S/N measured at the indicated wavelengths, in Column 12-13 we show whether or not the H_α and Li lines have been detected.

Source	Date of observation [UT]	Exp. Time [$N_{\mathrm{exp}}\times$ s]			Slit width [″]			S/N @ λ [nm]			H_α	Li
		UVB	VIS	NIR	UVB	VIS	NIR	400	700	1000		
					Pr.Id. 299.C-5048 (PI Manara)							
CrA-31	2017-09-01T03:30:30.048	4x215	4x135	4x3x75	1.0	0.9	0.9	8	20	21	Y	Y
CrA-36	2017-09-17T02:22:50.221	4x600	4x690	4x3x250	1.0	0.9	0.9	0	0	23	Y	N
CrA-42	2017-09-09T02:14:39.978	4x630	4x700	4x3x250	1.0	0.9	0.9	0	0	1	N	N
CrA-45	2017-09-06T00:37:53.044	4x440	4x340	4x3x150	1.0	0.9	0.9	0	24	1110	Y	Y
					Pr.Id. 0101.C-0893 (PI Cazzoletti)							
CrA-1	2018-05-28T04:25:20.708	4x90	4x150	4x150	1.0	0.9	0.9	24	14	35	Y	Y
CrA-22	2018-06-14T06:36:52.359	4x190	4x250	4x250	1.0	0.9	0.9	3	20	58	Y	...
CrA-26	2018-06-12T05:54:41.945	4x190	4x250	4x250	1.0	0.9	0.9	0	2	13	Y	N
CrA-40	2018-05-26T08:08:42.457	4x190	4x250	4x250	1.0	0.9	0.9	1	56	69	Y	Y
CrA-47	2018-06-15T04:01:23.919	4x190	4x250	4x250	1.0	0.9	0.9	1	13	309	Y	Y
CrA-48	2018-05-26T05:05:48.019	4x190	4x250	4x250	1.0	0.9	0.9	11	21	20	Y	N
CrA-53	2018-05-26T06:41:48.012	4x190	4x250	4x250	1.0	0.9	0.9	1	14	52	Y	Y
CrA-57	2018-05-27T05:18:45.651	4x90	4x150	4x150	1.0	0.9	0.9	3	17	83	Y	Y
IRS10	2018-06-11T06:08:20.787	4x190	4x250	4x250	1.0	0.9	0.9	0	0	2	N	N

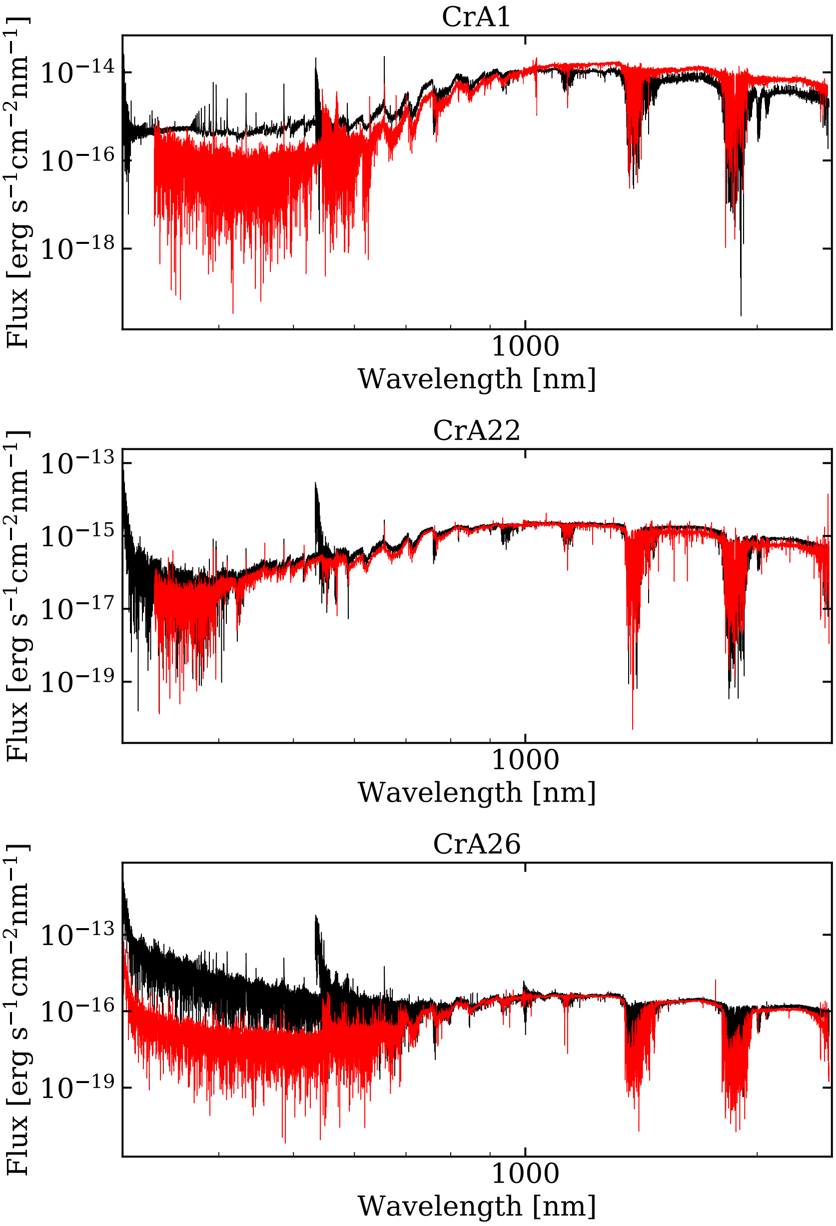

Figure 6.8: Spectra observed in our X-Shooter programs (black) along with a template with the same Spectral Type (red). The name of the sources is in the title of each subfigure. The absolute flux of each template was normalized to the flux of the observation at $\lambda = 1\mu m$.

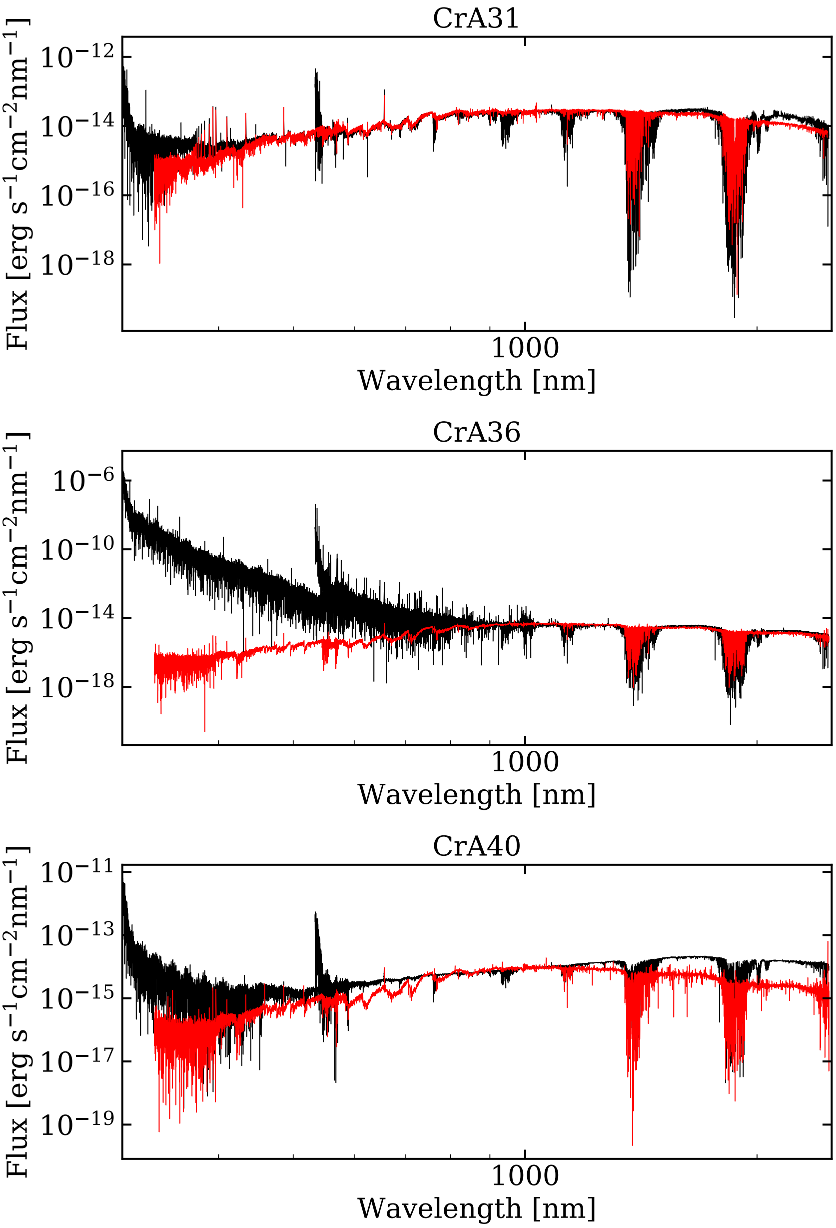

Figure 6.8: Continued

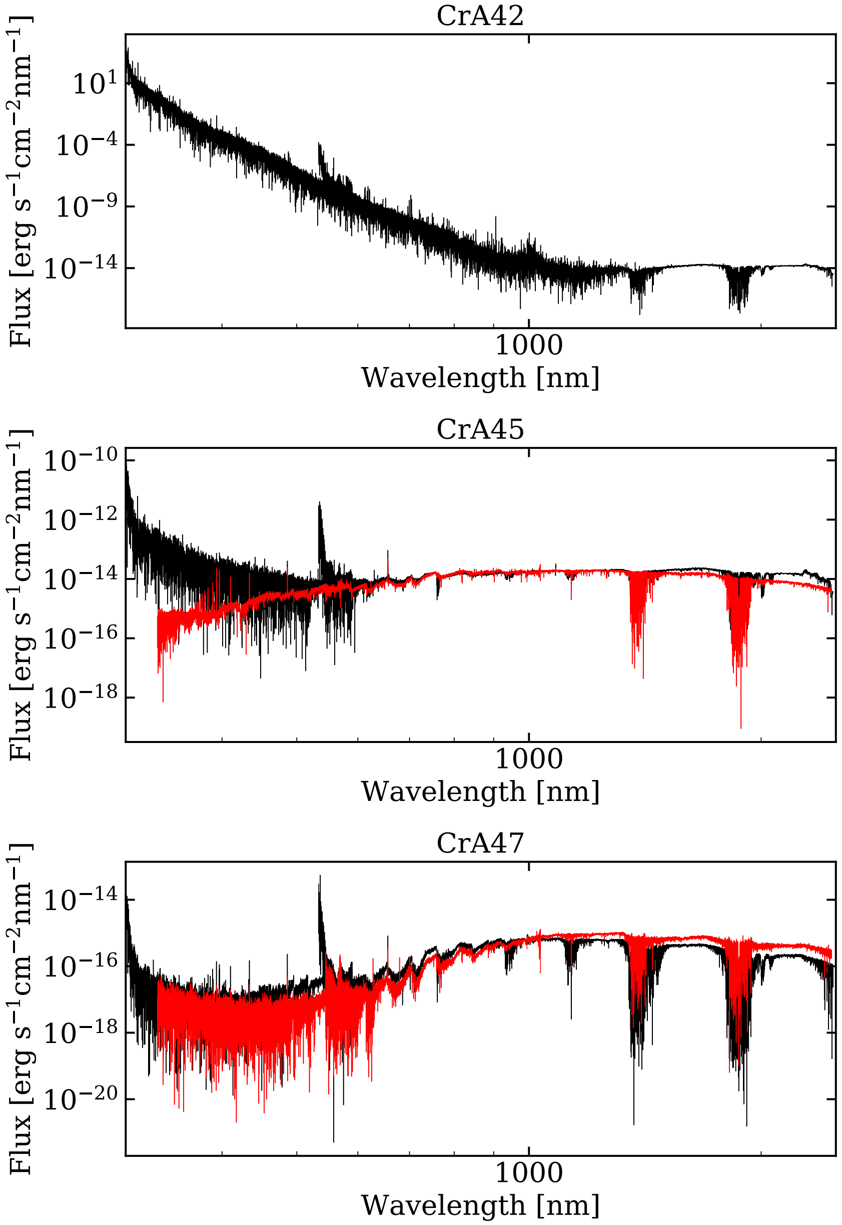

Figure 6.8: Continued

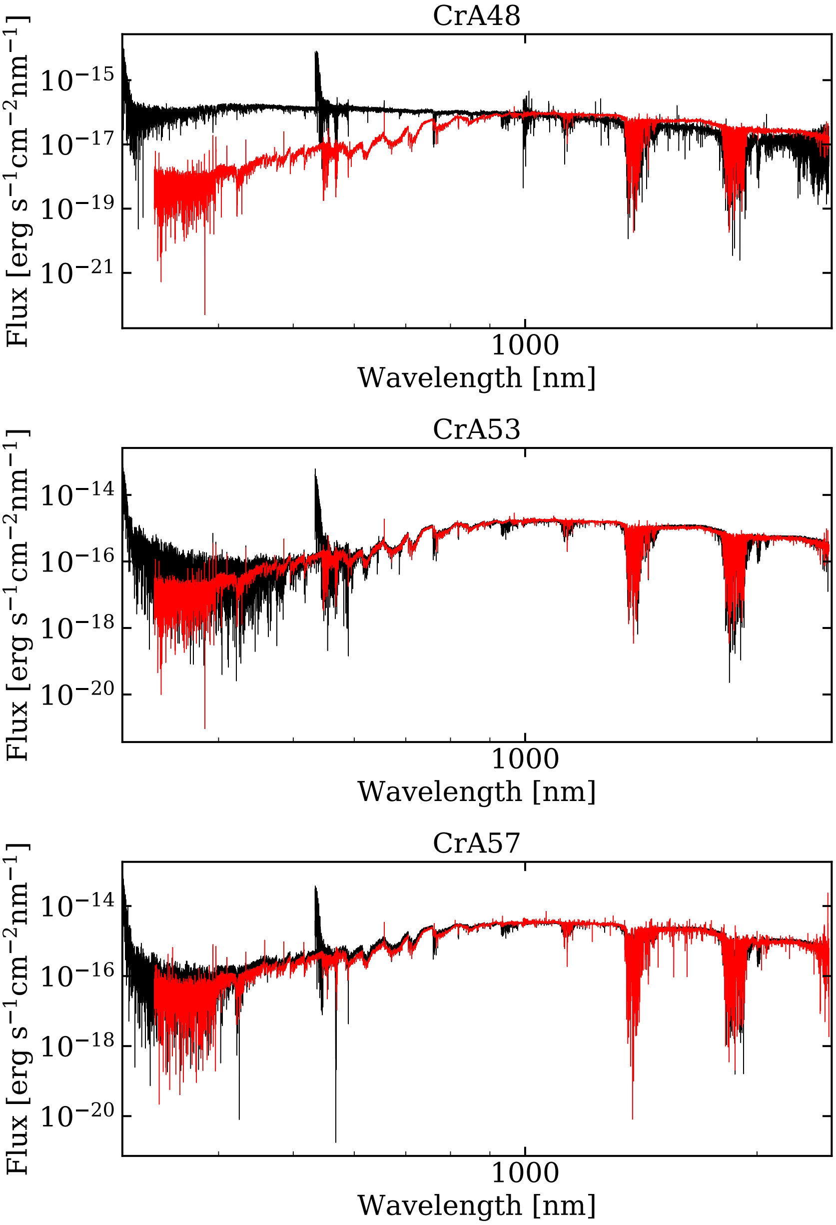

Figure 6.8: Continued

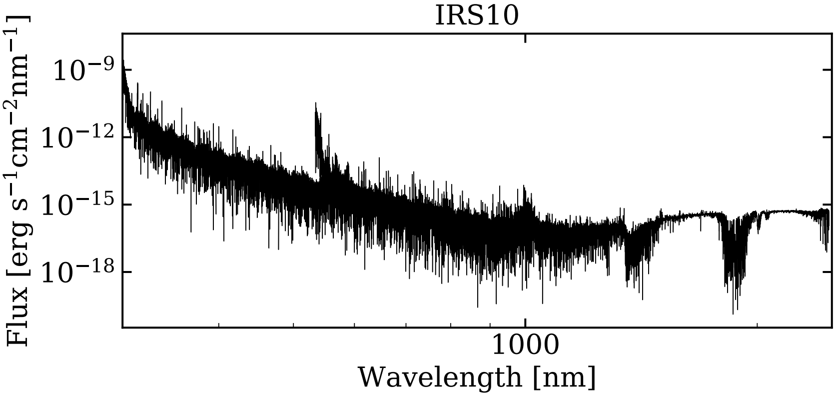

Figure 6.8: Continued

Acknowledgements. We thank S. van Terwisga, S. Andrews, G. Lodato and A. Hacar for very useful discussion, and Dr. Mark Gurwell for compiling the SMA Calibrator List (http://sma1.sma.hawaii.edu/callist/callist.html). We also acknowledge the DDT Committee and the Director of the La Silla and Paranal Observatory for granting DDT time. This work was partly supported by the Italian Ministero dell'Istruzione, Università e Ricerca through the grant Progetti Premiali 2012 – iALMA (CUP C52I13000140001), by the Deutsche Forschungs-gemeinschaft (DFG, German Research Foundation) - Ref no. FOR 2634/1 TE 1024/1-1, and by the DFG cluster of excellence Origin and Structure of the Universe (www.universe-cluster.de). This project has received funding from the European Union's Horizon 2020 research and innovation programme under the Marie Skłodowska-Curie grant agreement No 823823. H.B.L. is supported by the Ministry of Science and Technology (MoST) of Taiwan (Grant Nos. 108-2112-M-001-002-MY3 and 108-2923-M-001-006-MY3). J.M.A. acknowledges financial support from the project PRIN-INAF 2016 The Cradle of Life—GENESIS-SKA (General Conditions in Early Planetary Systems for the rise of life with SKA). C.F.M. and S.F. acknowledge an ESO Fellowship. M.T. has been supported by the DISCSIM project, grant agreement 341137 funded by the European Research Council under ERC-2013-ADG and by the UK Science and Technology research Council (STFC). Y.H. is supported by the Jet Propulsion Laboratory, California Institute of Technology, under a contract with the National Aeronautics and Space Administration. C.C.G and R.G.M acknowledge financial support from DGAPA UNAM. This paper makes use of the following ALMA data: ADS/JAO.ALMA#2015.1.01058.S. ALMA is a partnership of ESO (representing its member states), NSF (USA) and

NINS (Japan), together with NRC (Canada) and NSC and ASIAA (Taiwan), in cooperation with the Republic of Chile. The Joint ALMA Observatory is operated by ESO, AUI/NRAO and NAOJ. All the figures were generated with the `python`-based package `matplotlib` (Hunter, 2007).